Sustainable Energy & Fuels

ROYAL SOCIETY OF CHEMISTRY

PAPER

View Article Online
View Journal | View Issue

Cite this: *Sustainable Energy Fuels*, 2025, **9**, 5635

A co-doping strategy for p- to n-type transition and performance boost in SnSe-based flexible thermoelectric generators

Manasa R. Shankar,[a] A. N. Prabhu *[a] and Ramakrishna Nayak[b]

Flexible thermoelectric generators (FTEGs) have garnered considerable interest for their potential in energy harvesting applications. This study investigates the synthesis of SnSe and Bi/Te co-doped SnSe polycrystals using the solid-state reaction method, followed by the fabrication of FTEGs using a low-cost, scalable screen-printing technique. Hall effect measurements confirm successful doping, resulting in a transition from p-type to n-type conduction in SnSe. The Seebeck coefficient of the 2% Bi-doped SnSe/SnSe (p–n type) FTEG reaches −1146 μV K^{-1}, enhancing the thermoelectric performance. A maximum power output of 6.8 nW was obtained for a p–n-type FTEG consisting of SnSe and $Sn_{0.98}Bi_{0.02}Se_{0.97}Te_{0.03}$ at a temperature difference of 120 °C. Thermal conductivity measurements indicate that doping reduces phonon transport due to increased microstrain and dislocation density, which enhance phonon scattering. Furthermore, the FTEGs exhibited excellent mechanical stability, with less than 0.5% change in electrical resistance at bending angles up to 120° and after 500 cycles. These results suggest that Bi/Te co-doped SnSe is a potential candidate for scalable, flexible thermoelectric applications.

Received 5th February 2025
Accepted 19th August 2025

DOI: 10.1039/d5se00175g

rsc.li/sustainable-energy

1 Introduction

The rapid expansion of wearable and portable electronic devices has created a growing need for flexible, lightweight, and efficient energy-harvesting systems.[1] Among the diverse range of energy harvesting technologies, thermoelectric generators (TEGs) stand out due to their intrinsic capability to directly convert thermal gradients into electrical energy *via* the Seebeck effect.[2] This attribute is particularly advantageous when power autonomy is crucial, such as in wearable electronics, biomedical sensors, and flexible electronic devices. TEGs are solid-state devices known for their high reliability, minimal maintenance, and ability to recover electrical energy from waste heat without needing mechanical parts, liquids, or gases.[3] This makes them a potentially environmentally friendly alternative to traditional batteries, often requiring frequent replacement and posing environmental hazards.[4]

Traditionally, thermoelectric research has concentrated on chalcogen compounds such as Bi_2Te_3 [5] and PbTe,[6] which are used for low- and medium-temperature applications, respectively. However, the scarcity of tellurium (Te) in the Earth's crust has constrained the commercial viability of these generators, limiting their application in niche areas such as space exploration, watches, and Peltier coolers.[7] Despite investigations into alternative materials like oxides,[8] silicides, and half-Heuslers,[9] these materials generally exhibit lower thermoelectric performance (*ZT*) compared to their Te-based counterparts, thus curtailing their broader adoption. Conventional thermoelectric materials, however, are predominantly characterized by their rigidity and brittleness, which significantly hinders their deployment in flexible and stretchable applications. To address these limitations, recent research has increasingly focused on developing flexible thermoelectric materials that maintain high thermoelectric performance while offering mechanical compliance.[10] Among these, tin selenide (SnSe) stands out due to its exceptional thermoelectric properties, including a notably high Seebeck coefficient and intrinsically low thermal conductivity; both are critical for achieving high-efficiency energy conversion.[11,12] SnSe, a tellurium-free compound, has garnered significant interest within the thermoelectric community, having demonstrated a *ZT* of 2.6 in single crystal ingots along a preferential crystallographic plane.[12]

In the present study, SnSe samples were prepared through the solid-state reaction method, and their thermoelectric properties were further optimized through the strategic co-doping of bismuth (Bi) and tellurium (Te). The pristine SnSe exhibits p-type semiconducting behavior, while the Bi/Te-doped SnSe transitions to an n-type semiconductor. We initially fabricated and characterized separate n-type and p-type FTEGs. Subsequently, these n-type and p-type materials were combined to create a new flexible thermoelectric generator (FTEG) utilizing the screen-printing technique, which was then characterized to evaluate its performance. The screen-printing

[a]*Department of Physics, Manipal Institute of Technology, Manipal Academy of Higher Education, Manipal, 576104, India. E-mail: ashwatha.prabhu@manipal.edu*
[b]*Department of Humanities and Management, Manipal Institute of Technology, Manipal Academy of Higher Education, Manipal, 576104, Karnataka, India*

process offers several key advantages, including cost-effectiveness, simplicity, scalability, mass-production capability, and the ability to deposit thermoelectric materials onto flexible substrates. Additionally, unlike many traditional fabrication techniques for SnSe, such as solvothermal synthesis,[13] melting followed by spark plasma sintering (SPS),[14] and thermal evaporation,[15] which require high temperatures, high pressures, and lengthy fabrication times, screen printing can be performed at room temperature and atmospheric pressure. By addressing the challenges associated with merging mechanical flexibility with high thermoelectric efficiency, this study contributes to the advancement of flexible energy harvesting technologies. This work also reports the fabrication and optimization of FTEG devices using low-cost and sustainable materials and methods.

2 Materials and methods

2.1 Materials

The materials employed in this study included tin, selenium, and tellurium, all with 99.9% purity, purchased from Molychem, Mumbai, India, and bismuth with 99.999% purity from Otto Kemi, Maharashtra, India. The process also involved the use of diacetone alcohol from Loba Chemicals and cellulose acetate propionate from Sigma-Aldrich. The flexible thermoelectric generator (FTEG) was fabricated on a transparent, flexible polyester terephthalate (PET) film, 100 μm thick, provided by Venlon Polyester Film Ltd, India. Screen-printable silver ink, specifically Loctite ECI 1010 E&C, was obtained from Henkel, India.

2.2 Synthesis and characterization of SnSe and Bi/Te co-doped SnSe samples

A solid-state reaction method is employed to synthesize $Sn_{1-x}Bi_xSe_{0.97}Te_{0.03}$ (x = 0, 0.02, 0.04) polycrystals. Initially, high-purity precursor materials, including tin, selenium, bismuth, and tellurium, were combined in precise stoichiometric ratios and mixed thoroughly for two hours in an agate mortar using intense grinding. The homogeneous fine powder was then pelletized under a compression pressure of 5 tons, resulting in pellets with dimensions of 10 × 2 × 5 mm^3. These pellets were sintered at 400 °C for 24 hours in a quartz tube with a diameter of 12 mm, which was evacuated to a vacuum of 10^{-4} torr. After sintering, the furnace was permitted to cool down naturally to room temperature. The resulting $Sn_{1-x}Bi_xSe_{0.97}Te_{0.03}$ (x = 0, 0.02, 0.04) materials were formed into rectangular bulk samples, which were ground for further characterization. Fig. 1 provides a detailed illustration of the sample preparation process.[16] The structural characterization of SnSe and co-doped SnSe was performed using X-ray diffraction (XRD) using a Rigaku Ultima IV instrument, with a scan range of 10° to 90° and a step size of 0.02° per minute. The surface morphology of the prepared pellets was examined using a scanning electron microscope (SEM, Carl Zeiss Sigma).

2.3 Screen printing workflow

The screen-printing technique consists of a sequence of key procedures. Initially, the ink formulation is prepared. This ink is then applied to a screen, consisting of a fabric mesh stencil. A coating blade evenly distributes the ink across the screen surface, ensuring that it fills the mesh openings. A squeegee is then employed to apply pressure against the screen, forcing the ink through the mesh and onto the substrate. As the squeegee is drawn across the screen, it deposits a uniform layer of ink onto the substrate in the desired pattern. Upon removal of the screen, the inked pattern is transferred onto the substrate. Fig. 2 shows the schematic workflow of the screen-printing technique for the fabrication of the FTEG.

2.4 Ink formulation of SnSe and Bi/Te co-doped SnSe and characterization

Following the preparation of the bulk materials, these SnSe and Bi/Te co-doped SnSe samples were further processed to formulate inks suitable for screen printing. To achieve this, 20% cellulose acetate propionate (CAP) was dissolved in 80% diacetone alcohol, serving as the ink vehicle. Table 1 presents the composition of the three distinct Bi/Te co-doped $Sn_{1-x}Bi_xSe_{0.97}Te_{0.03}$ (x = 0, 0.02, 0.04) inks. The ink mixtures were homogenized using a magnetic stirrer for one hour to ensure uniform distribution of the components. Ink viscosity was controlled within the ideal range of 1750–2000 cP to ensure compatibility with screen printing.

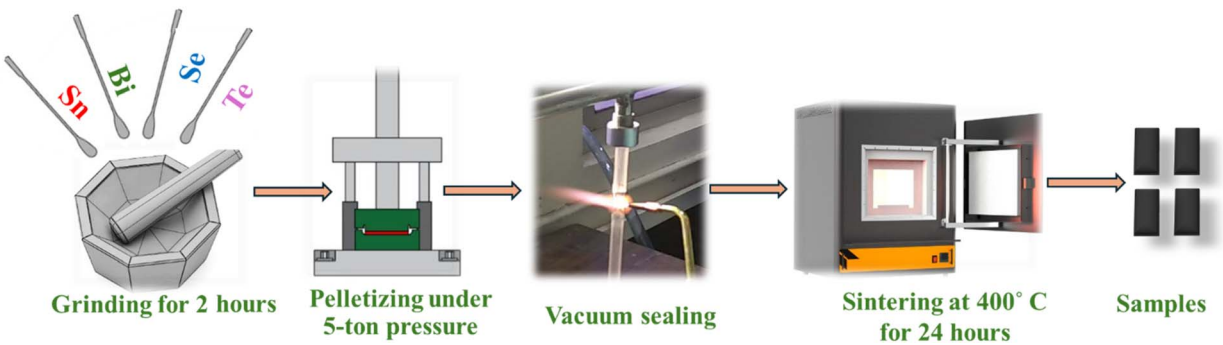

Fig. 1 The sequential process of the solid-state reaction method for synthesizing SnSe and co-doped SnSe materials.

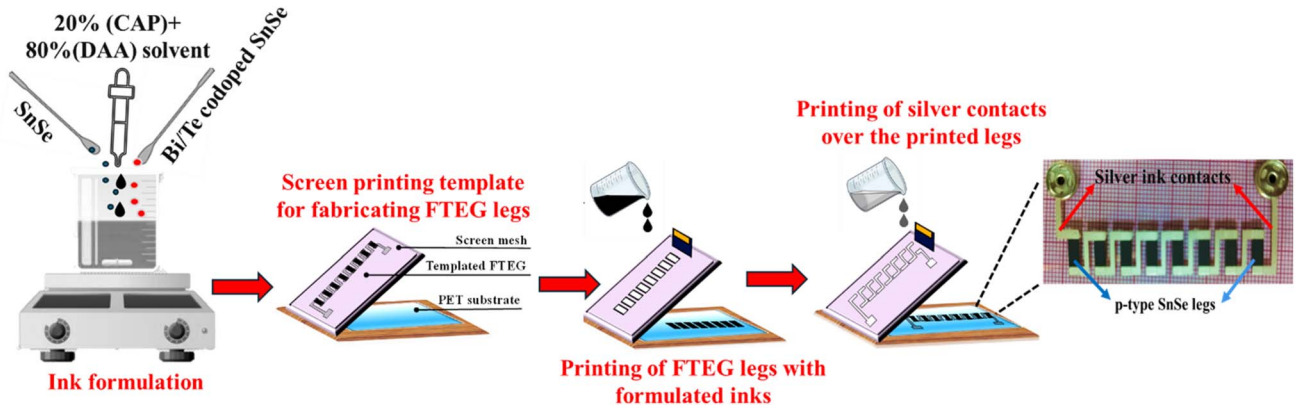

Fig. 2 Schematic workflow of the screen-printing technique for the fabrication of the FTEG.

Table 1 Composition of SnSe and codoped SnSe inks

Sample	Sn (g)	Se (g)	Bi (g)	Te (g)	Ink vehicle (g)
SnSe	3.002	1.997	—	—	1.75
$Sn_{0.98}Bi_{0.02}Se_{0.97}Te_{0.03}$	2.895	1.906	0.103	0.096	1.75
$Sn_{0.96}Bi_{0.04}Se_{0.97}Te_{0.03}$	2.810	1.889	0.206	0.095	1.75

The crystallinity of the inks was characterized using a Rigaku Ultima IV X-ray diffraction (XRD) instrument, with a scanning range of 10° to 90° and a step size of 0.02° min^{-1}. The morphology of the prepared inks was examined using a scanning electron microscope (SEM, Carl Zeiss Sigma). The ink samples were pelletized using a hydraulic press at 5 tons of pressure for a duration of 5 minutes. These pellets were then analyzed for their electrical properties through Hall effect measurement using a Keithley Hall measurement system, employing the Van der Pauw method at room temperature.

2.5 Screen printing of FTEGs

To develop flexible thermoelectric generators (FTEGs) using specially formulated inks, separate p-type and n-type FTEGs were initially fabricated, each consisting of eight legs measuring 3 mm × 10 mm (see Fig. 3(a and b)). A mesh screen with a mesh count of 120 cm^{-1} (Shebro, INDIA) was employed, and the stencil was created using a combination of direct and indirect techniques.[17] A flat, wedge-shaped rubber squeegee with a hardness of 75 Shore A was used to apply multiple overprints (12 layers) of the respective p-type and n-type inks (refer to Table 1). Additionally, commercially available silver ink was screen printed as electrodes on both the p-type and n-type devices. Subsequently, a combined p–n type FTEG was fabricated using

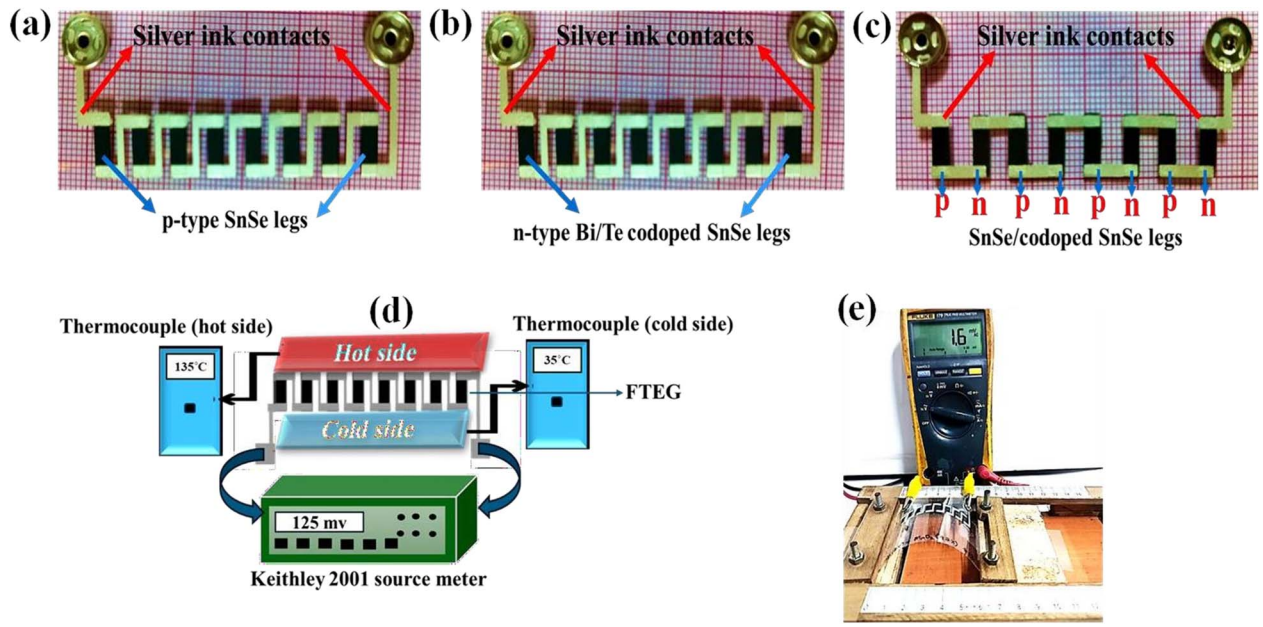

Fig. 3 (a) FTEG with p-type legs, (b) FTEG with n-type legs, (c) FTEG with alternative p–n type legs, (d) characterization arrangement for the FTEG, and (e) setup for the FTEG's flexibility analysis.

the same inks (Fig. 3c), interconnecting the p-type and n-type legs with four layers of silver ink screen printed onto a 100 μm thick flexible PET substrate. All FTEGs were fabricated to have the same dimensions of 15 mm × 55 mm.

2.6 Characterization of the FTEG

A customized experimental setup consisting of two thermocouples and a Keithley 2001 source meter (illustrated in Fig. 3d) was utilized to determine the Seebeck coefficient and power output of the FTEGs based on SnSe and Bi/Te codoped SnSe inks. One side of the FTEG was heated *via* a hot plate to create a temperature gradient, whereas the opposite remained at room temperature. The temperatures at both ends of the FTEG were recorded using a K-type digital thermocouple (Lutron TM-902C). As previously documented, the Keithley 2001 source meter records both the voltage generated across the FTEG and its internal electrical resistance.[18–20] A Mitutoyo 547–301 Digimatic thickness gauge was employed to measure the thickness of the ink film. The flexibility of the FTEGs was tested at ambient temperature using a two-probe multimeter (Fluke 179)

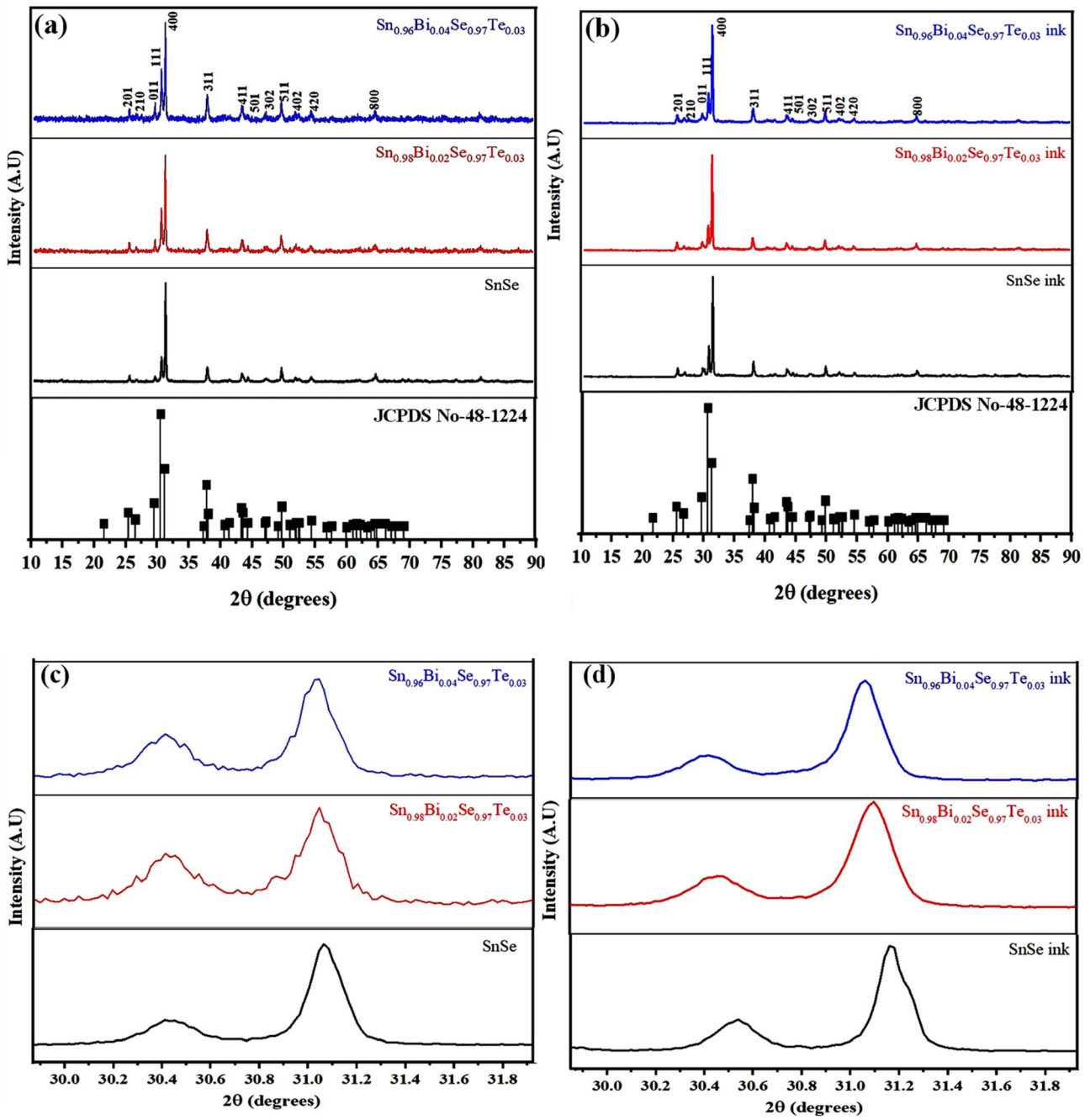

Fig. 4 (a) XRD peak pattern of powder, (b) XRD peak pattern of ink-based samples, (c) peak shift graph of powder samples, and (d) peak shift graph of ink-based samples.

in conjunction with a specially designed bending device (Fig. 3e).[21] Additionally, an evaluation of the thermoelectric performance was conducted after subjecting the FTEGs to various single-fold bending cycles (0, 100, 200, 300, 400, and 500).

3 Results and discussion

3.1 Structural evaluation *via* X-ray diffraction analysis

The X-ray diffraction (XRD) analysis of pellet powder and ink-based SnSe/Bi–Te co-doped SnSe powder (prepared by adding 20% cellulose acetate propionate (CAP) and 80% diacetone alcohol as the ink vehicle) reveals similar peak patterns, indicating that the addition of the ink vehicle did not affect the crystal structure of the material. As seen in Fig. 4a and b, all the diffraction peaks matched with the JCPDS data (48-1224) without any secondary phases within the detectable range of the analysis,[22] confirming that all prepared samples are single-phase and correspond to the intended composition. The (400) plane exhibited the most intense diffraction peak across all samples, denoting the sample's preferred growth orientation. All samples crystallize in the low-temperature orthorhombic phase of SnSe, associated with the *Pnma* space group.[23] The orthorhombic crystal structure of SnSe is retained across both preparation methods.

Fig. 4c and d show a noticeable shift towards the lower angle side in the high-intensity peak pattern at (400), which is observed upon doping SnSe with Bi/Te. This shift suggests lattice expansion due to the substitution of Sn atoms by the larger Bi and Te atoms, leading to increased interplanar spacing.[24] The observed peak shifts in the XRD spectrum arise from the slight variation in ionic radii between Bi (230 pm) and Sn (225 pm), causing strain in the matrix.[16] The difference of 5 pm in ionic radii results in tensile stress within the compounds. The variation in lattice parameters tabulated in Table 2 confirms the correlation between increasing Bi content and the observed peak shifts. These results indicate successful incorporation of dopant atoms into the SnSe lattice. We adopted the Scherrer method to determine the crystallite size (D) and strain (ε). The Scherrer equation is given by eqn (1),[25]

$$D = \frac{0.9\ \lambda}{\beta \cos \theta} \quad (1)$$

considering the X-ray wavelength (λ), full width at half maximum (β), and peak position (θ) in radians. Dislocation refers to flaws or irregularities in the crystal structure. However, the addition of Bi/Te has increased dislocation density and microstrain. The dislocation density (δ) can be determined using eqn (2),[25]

$$\delta = \frac{1}{D^2} \quad (2)$$

Similarly, eqn (3) was utilized to calculate the average microstrain (ε) present in the samples,[25]

$$\varepsilon = \frac{\beta}{4 \tan \theta} \quad (3)$$

The changes in crystallite size, dislocation density, and microstrain, as demonstrated in Table 2, are well aligned with earlier reports.[26] Materials with smaller crystallite size, elevated dislocation density, and higher microstrain typically show reduced thermal conductivity.[27] Dislocation plays a crucial role in thermoelectric properties, as it can impact both charge carrier flow and heat transfer within the material. These factors are interrelated: as crystallite size decreases, dislocation density and microstrain tend to rise due to an increase in grain boundaries, which introduce more defects.

3.2 SEM and EDAX studies of screen-printed ink films

Scanning electron microscopy (SEM) was employed to study the microstructural properties of the samples, as depicted in Fig. 5a–f. The SEM images of the pellet samples with a magnification scale of approximately 1 μm made from SnSe and Bi/Te co-doped SnSe (Fig. 5a–c) using the solid-state reaction method exhibit a relatively smooth and uniform surface texture characterized by fine granulation. This uniform morphology indicates effective particle interconnection, essential for optimizing thermoelectric performance.[28] The observed layered structure suggests a well-organized arrangement of the material that can enhance carrier mobility. Distinct crystal boundaries may influence the scattering of charge carriers and phonons, thereby affecting both electrical and thermal conductivity. The compactness of the structure also implies good mechanical integrity, crucial for the stability of thermoelectric devices during operation.

After grinding the sintered pellets into fine powder, the material was used to fabricate screen-printed FTEGs. The corresponding SEM images of the printed films after thermal annealing are shown in Fig. 5d–f, captured at a magnification

Table 2 Powder XRD analysis of SnSe and Bi/Te co-doped SnSe: structural characterization of powder and ink-based samples

Sample	Average crystallite size (D) (nm)	a (Å)	b (Å)	c (Å)	Dislocation density (δ) 10^{15} m^{-2}	Microstrain (ε) 10^{-3}
SnSe	30 ± 3	11.490	4.151	4.432	1.1	3.7
$Sn_{0.98}Bi_{0.02}Se_{0.97}Te_{0.03}$	28 ± 2	11.505	4.153	4.434	1.3	4.3
$Sn_{0.96}Bi_{0.04}Se_{0.97}Te_{0.03}$	27 ± 2	11.520	4.158	4.438	1.4	4.7
SnSe ink	29 ± 3	11.495	4.150	4.432	1.2	4.0
$Sn_{0.98}Bi_{0.02}Se_{0.97}Te_{0.03}$ ink	24 ± 2	11.510	4.154	4.433	1.7	5.6
$Sn_{0.96}Bi_{0.04}Se_{0.97}Te_{0.03}$ ink	23 ± 2	11.515	4.157	4.439	1.9	6.3

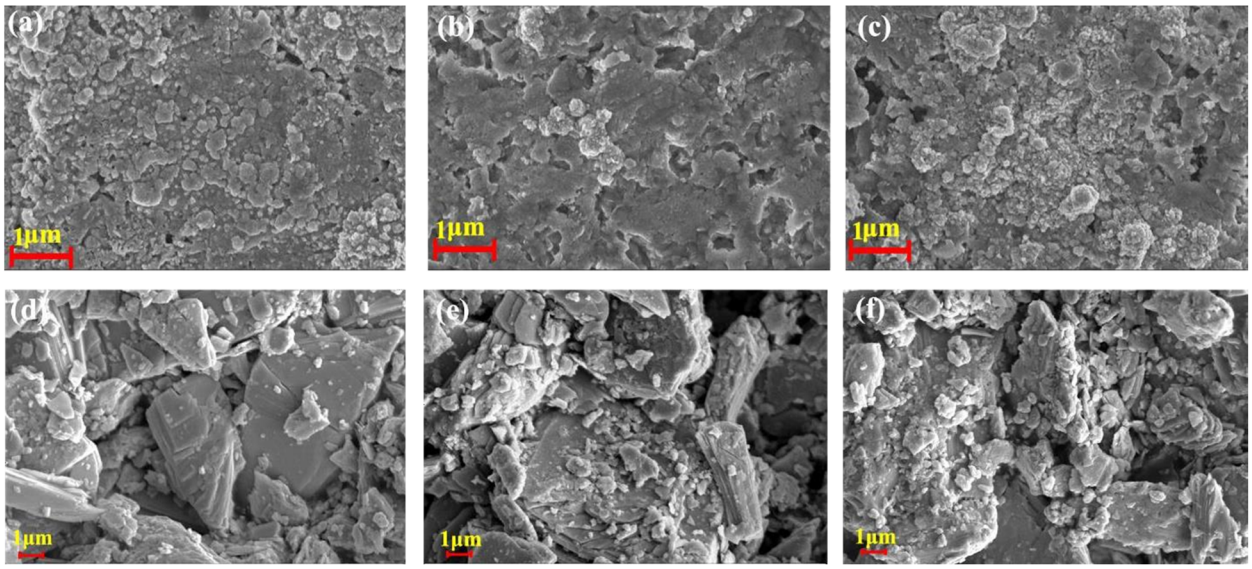

Fig. 5 SEM images of (a) SnSe, (b) $Sn_{0.98}Bi_{0.02}Se_{0.97}Te_{0.03}$, and (c) $Sn_{0.96}Bi_{0.04}Se_{0.97}Te_{0.03}$ pellet samples, and SEM images of (d) SnSe, (e) $Sn_{0.98}Bi_{0.02}Se_{0.97}Te_{0.03}$, and (f) $Sn_{0.96}Bi_{0.04}Se_{0.97}Te_{0.03}$ ink-film samples.

corresponding to a 1 μm scale to reveal surface morphological features. The presence of a layered structure and different particle morphologies may facilitate phonon scattering, which is advantageous for achieving low thermal conductivity while maintaining adequate electrical conductivity.[29] The rougher texture observed in the printed samples can enhance interfacial contact between the thermoelectric material and the substrate, thus improving overall device performance. Additionally, any

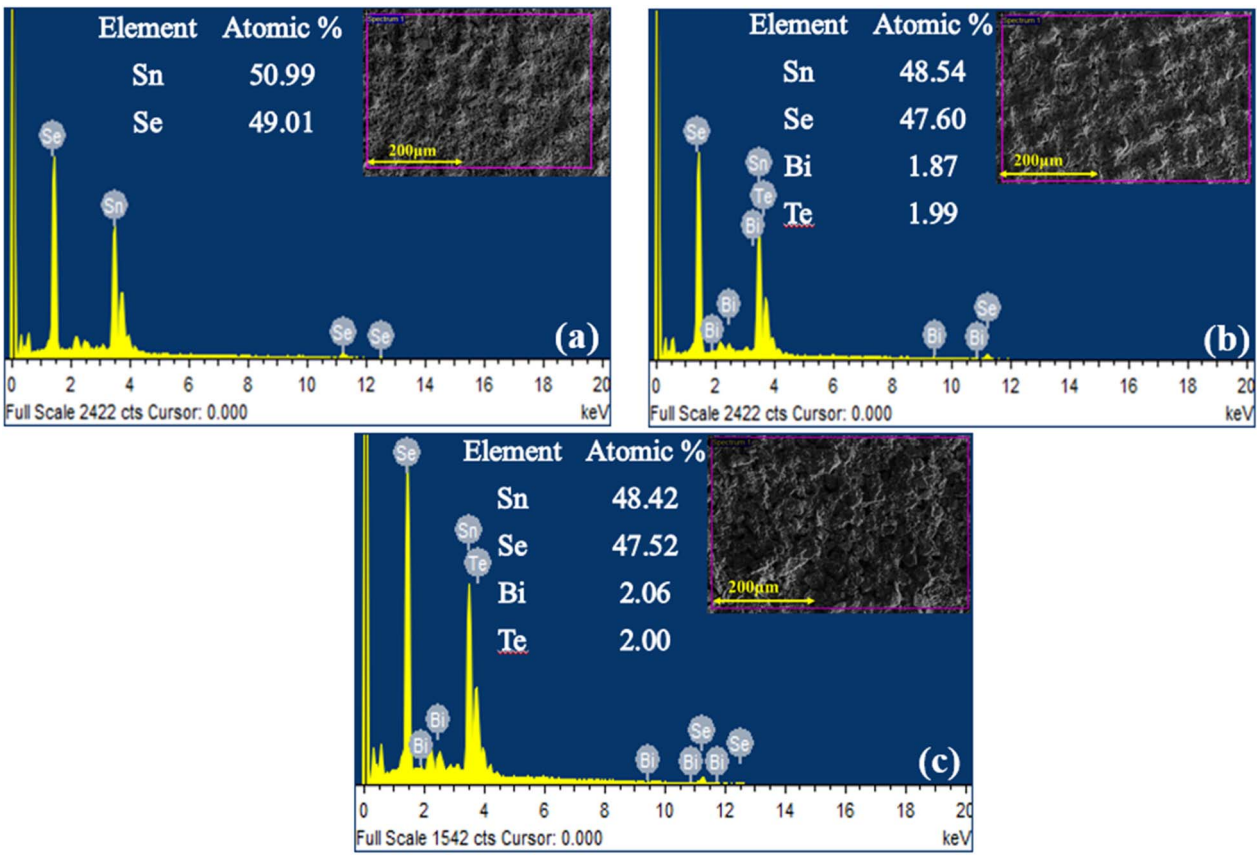

Fig. 6 EDAX images with precise locations of spectrum acquisition of (a) SnSe, (b) $Sn_{0.98}Bi_{0.02}Se_{0.97}Te_{0.03}$ and (c) $Sn_{0.96}Bi_{0.04}Se_{0.97}Te_{0.03}$ ink-film samples.

visible cracks or voids may serve as potential points for phonon scattering, further contributing to thermoelectric efficiency. The bulk samples exhibit densely packed grains with relatively uniform morphology, while the printed films appear less compact and structurally more porous, likely due to the nature of the screen-printing process and post-deposition drying limitations. Overall, the SEM analysis highlights distinct microstructural characteristics between the pellet samples and the printed FTEGs. The uniform structure of the pellets shows high material quality, while the varied structure of the printed devices enables tunable thermoelectric properties in flexible applications.

The EDAX spectra obtained from the ink films reveal their elemental compositions, accompanied by inset images indicating the precise spectrum acquisition locations with a magnification scale of 200 μm. The SnSe sample displays a nearly stoichiometric ratio of Sn and Se (Fig. 6a), while the Bi/Te co-doped SnSe ink films confirm the successful integration of Bi and Te alongside substantial amounts of Sn and Se (Fig. 6(b and c)). This elemental distribution aligns with the intended doping concentrations, thereby facilitating the anticipated enhancement in the thermoelectric properties of the materials.

Fig. 7a illustrates the thickness measurement of the SnSe and Bi/Te co-doped SnSe ink films. The data reveal that the maximum observed variation in thickness does not exceed 2%, underscoring the consistency and reliability of the film deposition process.

3.3 Hall effect study

Hall effect measurements were conducted at an ambient temperature of 300 K to assess the impact of Bi and Te doping on the carrier concentration, type, and mobility in SnSe samples. The result shown in Fig. 7b reveals that pure SnSe behaves as a p-type semiconductor,[30] as evidenced by its positive carrier concentration. However, with the introduction of dopants, the samples display n-type behavior, represented by the negative sign of the carrier concentration.[12] These findings are consistent with Seebeck coefficient measurements. Fig. 7b also illustrates the effect of dopant concentration on both mobility and carrier concentration. As the concentration of Bi increases, mobility decreases, likely due to the enhanced scattering of carriers. It is also evident that mobility and carrier concentration follow opposing trends, as reported in previous studies.[31] Upon introducing an n-type dopant like Bi to the p-type SnSe matrix, electrons introduced by the dopant shift the majority carrier from holes to electrons. This transition reduces the carrier concentration from $+4.28 \times 10^{16}$ cm^{-3} (in undoped SnSe) to -0.708×10^{16} cm^{-3} in a sample doped with 2% Bi ($Sn_{0.98}Bi_{0.02}Se_{0.97}Te_{0.03}$). With further increase in Bi concentration, the material maintains its n-type behavior, and the carrier concentration rises to -1.78×10^{16} cm^{-3} in the 4% Bi-doped sample. Te, which partially substitutes for Se, plays a supportive role by slightly modifying the band structure and defect chemistry, thereby facilitating n-type conduction and influencing carrier scattering behavior.[32] Initially, the neutralization of p-type defects by n-type dopants reduces defect-induced scattering and thus increases mobility. However, at higher doping levels, the increased carrier concentration contributes to enhanced electron–electron scattering, resulting in a subsequent decline in mobility.[33] These changes in carrier concentration and mobility are crucial for tuning the Seebeck coefficient and optimizing the thermoelectric performance of the material.

3.4 Transient thermal conductivity studies

Fig. 8a and b depict the variation in the specific resistance and transient thermal conductivity of the p-type, n-type, and p–n-type FTEGs across five different temperature gradients. The plots reveal that as the temperature increased, the specific resistance of the fabricated FTEGs decreased, which can be attributed to the increase in thermally excited charge carriers.[34] As the temperature rises, more electrons or holes are activated, leading to a higher carrier concentration. Although phonon

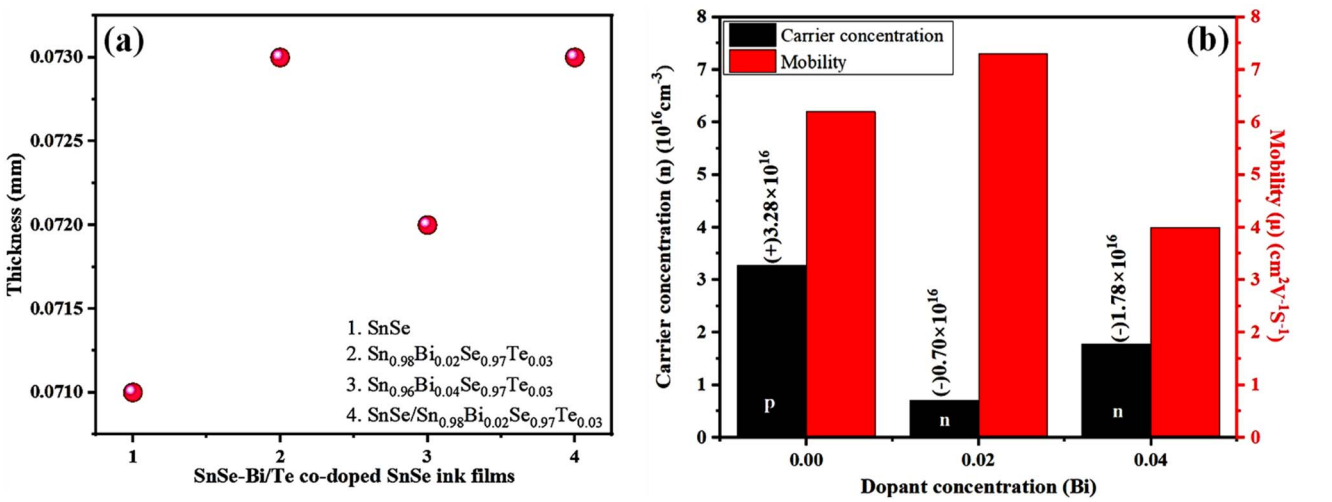

Fig. 7 (a) Thickness values and (b) carrier concentration and mobility graph of ink samples.

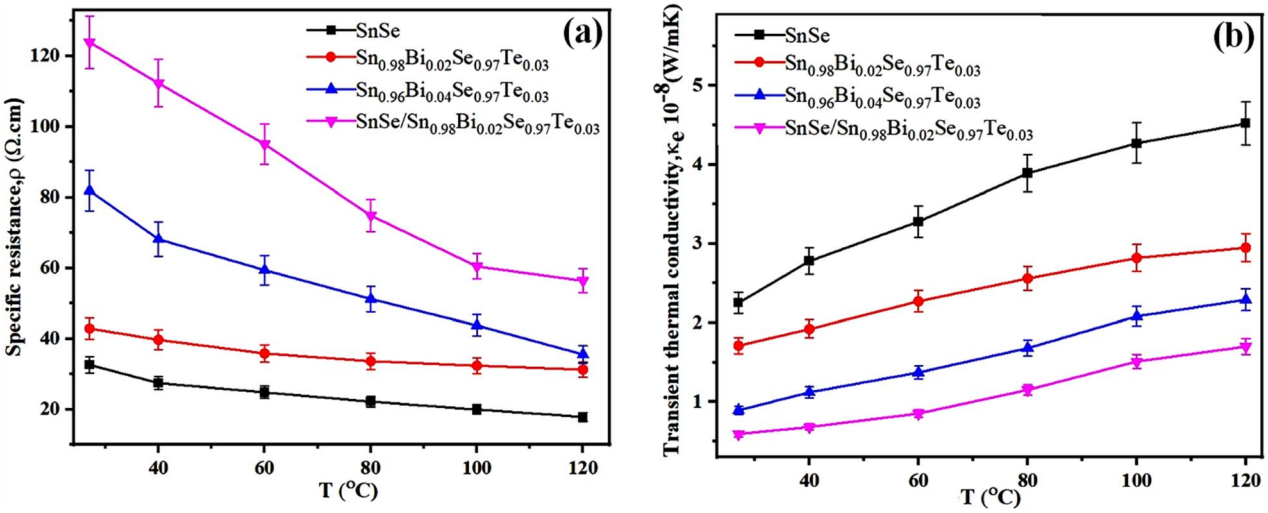

Fig. 8 (a) Specific resistance and (b) transient thermal conductivity (κ_e) graph of the fabricated FTEGs.

scattering generally intensifies at elevated temperatures, the increase in charge carriers compensates for this effect, resulting in an overall reduction in specific resistance. This behavior is typical in semiconductor-based thermoelectric materials.[35] Among the four FTEGs, the SnSe (p-type) FTEG exhibited the highest transient thermal conductivity of 4.52×10^{-8} W m^{-1} K^{-1}, while the $Sn_{0.98}Bi_{0.02}Se_{0.97}Te_{0.03}$, $Sn_{0.96}Bi_{0.02}Se_{0.97}Te_{0.03}$, and $SnSe/Sn_{0.98}Bi_{0.02}Se_{0.97}Te_{0.03}$ (p–n type) FTEGs demonstrated the lowest values. The FTEGs showed the lowest thermal conductivity, attributed to the increased microstrain and dislocation density in the Bi/Te-doped SnSe compared to undoped SnSe. These defects promote phonon scattering, reducing thermal transport.

This result correlates well with the XRD findings, where the introduction of Bi and Te dopants caused an increase in microstrain and dislocation density with significant variation in lattice parameters. The atomic size mismatch between the dopants and SnSe contributed to these changes, leading to greater defect formation. These microstructural defects, particularly dislocations, serve as effective phonon scattering centers, hindering thermal conductivity.

3.5 Electrical resistance, Seebeck coefficient, and power output studies

Fig. 9a illustrates the variation of electrical resistance as a function of the temperature difference (ΔT) in the fabricated FTEGs. It is observed that as ΔT increases, the electrical resistance of all FTEGs decreases, demonstrating semiconductor behavior, which is advantageous for thermoelectric applications.[36] Compared to the pristine SnSe FTEG with the Bi and Te doped FTEGs, the pristine SnSe FTEG displays lower electrical resistance. In contrast, increasing the concentration of dopants leads to a rise in electrical resistance. This increase can be attributed to changes in mobility and carrier concentration caused by the doping process. Specifically, higher doping levels can disrupt the transport of charge carriers, resulting in increased resistance. For this reason, the doping level has been limited to 4%, and based on this result, we opted to fabricate a p–n device using SnSe and a 2% Bi-doped sample. Additionally, introducing dopants can create defects within the crystal lattice, which can impede the flow of charge carriers.[37] Fig. 9b illustrates the internal voltage (ΔV) generated by the FTEGs at various temperature differences (ΔT). The results indicate a consistent increase in voltage output as temperature rises, which is characteristic of thermoelectric materials. This behavior occurs due to the enhanced thermal excitation of charge carriers that leads to greater mobility, resulting in increased voltage generation. Among the tested devices, the p–n $SnSe–Sn_{0.98}Bi_{0.02}Se_{0.97}Te_{0.03}$ FTEG shows the highest voltage output across all ΔT values, likely due to the effective integration of p-type and n-type semiconductors that promote efficient charge carrier transport.

The Seebeck coefficient of the FTEGs (Fig. 9c) was determined by applying a linear fit to the slope of the ΔV *versus* ΔT data. The pristine SnSe exhibited p-type behavior, characterized by positive thermopower, while the doped SnSe FTEGs displayed n-type behavior due to the additional charge carriers provided by Bi doping.[23] Te co-doping supported this transition by complementing the electronic effects of Bi and aiding in the stabilization of n-type conduction.[32] Notably, the p–n $SnSe/Sn_{0.98}Bi_{0.02}Se_{0.97}Te_{0.03}$ FTEG achieved the highest Seebeck coefficient at -1146 μV K^{-1}, reflecting enhanced thermoelectric performance due to the synergistic effect of p-type and n-type materials. In contrast, the 4% Bi-doped FTEG recorded the lowest Seebeck coefficient (-207 μV K^{-1}), which can be attributed to the increased carrier concentration resulting from higher doping levels. According to the Pisarenko relation,[38] the Seebeck coefficient decreases with increasing carrier concentration, consistent with our observations. Furthermore, the enhanced carrier–carrier and impurity scattering at high doping levels likely contribute to reduced mobility, collectively leading to the observed decline in thermopower. The power output (P) of the printed flexible thermoelectric generator can be determined using eqn (4):[17]

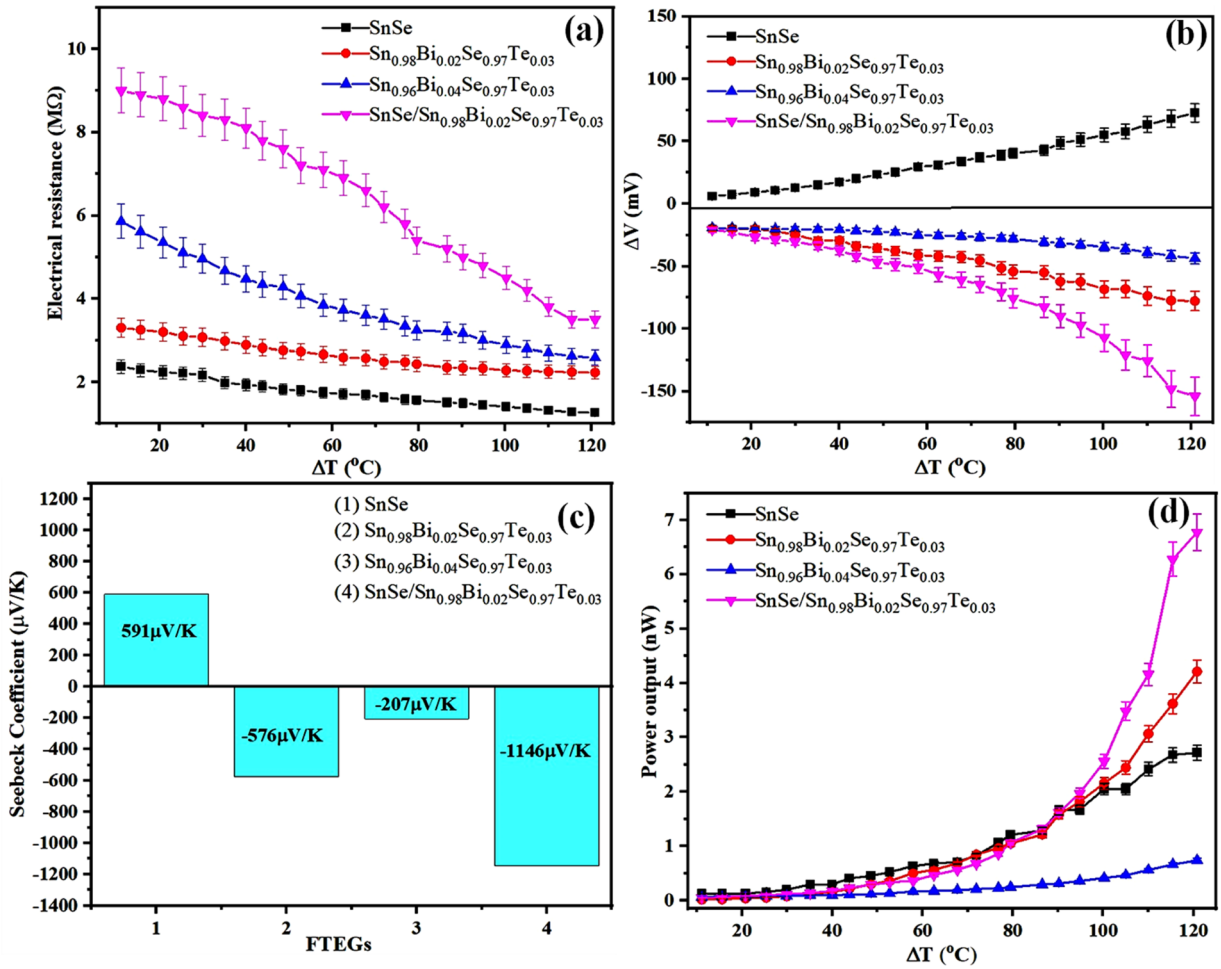

Fig. 9 (a) Electrical resistance, (b) Δ*V versus* Δ*T*, (c) Seebeck coefficient, and (d) power output plot of the fabricated FTEGs.

$$P = \frac{V^2}{R} \tag{4}$$

Here, V is the open-circuit voltage across the FTEG measured in volts at a specific temperature gradient, while R is the internal resistance of the FTEG in ohms. The estimated power outputs for the screen-printed p-type, n-type, and p–n-type FTEGs are depicted in Fig. 9d. The p–n type FTEG achieves the maximum power output of approximately 6.8 nW at a temperature difference (ΔT) of 120 °C. This optimal power output is primarily due to the increased internal voltage (Fig. 9b), Seebeck coefficient (Fig. 9c), and decreased transient thermal conductivity (Fig. 8b) in the p–n type FTEG. The combination of p-type and n-type materials considerably affects the thermoelectric properties, as their interaction enhances overall performance. Various factors account for the observed results. First, the presence of the p–n junction facilitates a higher voltage output, as the thermal gradient promotes charge separation, resulting in a greater potential difference across the junction.[39] Secondly, the synergistic effect of the p-type and n-type materials optimizes charge carrier dynamics, which improves energy conversion efficiency.[39] Lastly, the interplay between thermal and electrical properties in the combined materials enhances the overall power output of the p–n type FTEG, which is reflected in the significant performance observed at elevated temperature gradients.

Table 3 compares the power output of the p–n-type FTEG with some of the standard reported results.

3.6 Flexibility analysis of FTEGs

The flexibility and durability of the screen-printed FTEGs fabricated using SnSe and Bi/Te co-doped SnSe were rigorously evaluated using a customized bending apparatus (Fig. 3e). To assess the impact of mechanical stress on electrical performance, electrical resistance was measured at bending angles of 0°, 30°, 60°, 90°, and 120°. The results showed minimal variation in resistance across these angles, with a maximum deviation of less than 0.5% (Fig. 10a). This minimal change indicates that the FTEGs maintain their electrical integrity even when subjected to significant mechanical deformation. Furthermore, the stability of the devices was tested over multiple bending cycles, specifically after 0, 100, 300, 400, and 500 cycles, revealing only slight variation in internal resistance (Fig. 10b). These findings underscore the exceptional mechanical stability and flexibility of the SnSe and Bi/Te co-doped FTEGs,

Table 3 Reported power output of FTEGs: present work and literature comparison

FTEG material	Fabrication technique	Substrate	Number of leg couples	Seebeck coefficient ($\mu V\ K^{-1}$)	Power output (nW)	ΔT (K)	Ref.
PEDOT:PSS	Solution coating	Polyester fabric	5	18.5	12.29	75	40
PEDOT-Tos/carbon	Inkjet printing	Silicon	54	−48.0	1.13	308	41
PEDOT:PSS/Ag	Inkjet printing	Polyimide	8	—	0.24×10^{-3}	5	42
Sb_2Te_3/Bi_2Te_3	Deposition	Silk fabric	12	—	15.00	35	43
Ag_2Se/PVDF	Physical mixing + cold pressing	PI	5	95.9	5.00	30	44
Graphene	Printing	Paper	5	−21.5	1.70	60	45
Silver/nickel	Thermal evaporation	Fiber	7	—	2.00	6.6	46
$AuCl_3$-doped P3HT	Spin coating	Flip film	20	163.0	1.90	10	47
Cu_2Se	Magnetron sputtering + thermal evaporation	Kapton	10	55.0	3.30	38	48
MWCNT-NH_2/NiO	Screen printing	PET film	15	55.2	1.44	373	21
MWCNT-NH_2/CuO	Screen printing	PET film	15	47.7	1.06	373	21
MWCNT-NH_2/Fe_2O_3	Screen printing	PET film	15	43.3	0.32	373	21
SnSe/PEDOT:PSS/MWCNT/DMSO	Vacuum filtration	PI	5	22.3	14.70	39	49
SnSe–Bi/Te co-doped SnSe	Screen printing	PET film	8	1146.0	6.80	120	[a]

[a] Present work.

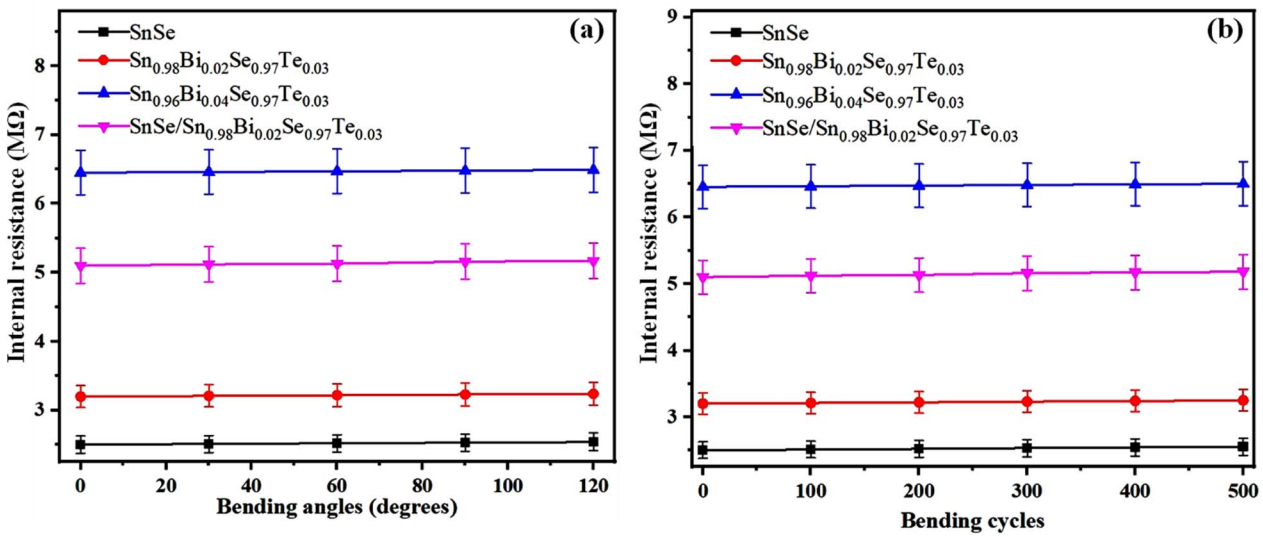

Fig. 10 (a) Internal resistance *vs.* bending angle and (b) internal resistance *vs.* bending cycles of the fabricated FTEGs.

confirming their robustness under repeated stress. As a result, these properties make them highly suitable for practical applications in wearable devices and flexible sensors, where reliability and durability are crucial for optimal performance in dynamic environments.

4 Conclusion

This study explores the thermoelectric performance of SnSe and Bi/Te-doped SnSe flexible thermoelectric generators (FTEGs), fabricated using a low-cost, scalable screen-printing technique. The SnSe and doped SnSe materials were synthesized using the solid-state reaction method, ensuring high purity and phase stability. Characterization techniques, including XRD, SEM, and EDAX, were employed to assess the structural integrity, morphology, and elemental composition. XRD analysis confirmed the successful incorporation of Bi and Te dopants into the SnSe matrix, leading to modified lattice parameters. SEM and EDAX results demonstrated uniform film morphology and consistent distribution of dopants. The Bi/Te co-doping facilitated a transition from p-type to n-type behavior, optimizing the carrier concentration and significantly enhancing the thermoelectric performance. The p–n-type SnSe/$Sn_{0.98}Bi_{0.02}Se_{0.97}Te_{0.03}$ FTEG achieved a peak Seebeck coefficient of $-1146\ \mu V\ K^{-1}$ and a power output of 6.8 nW at a 120 °C temperature gradient. Transient thermal conductivity measurements indicated a reduction in thermal conductivity, attributed to phonon scattering resulting from defects

introduced by Bi/Te doping. The FTEGs also demonstrated remarkable mechanical flexibility, retaining electrical stability even after 500 bending cycles, with less than 0.5% variation in resistance across different bending angles. These findings highlight the potential of screen-printed Bi/Te co-doped SnSe FTEGs for flexible thermoelectric energy harvesting, offering promising applications in wearable devices and flexible sensors. Future work will focus on optimizing the material composition and improving device efficiency for large-scale commercial usage.

Author contributions

Manasa R. Shankar: conceptualization, analysis, methodology, and original manuscript drafting. A. N. Prabhu: supervision, validation, manuscript review and editing, and resource allocation. Ramakrishna Nayak: resources, technical support, writing review & editing, and supervision.

Conflicts of interest

The authors state that there are no conflicts of interest to disclose.

Data availability

The corresponding author can provide the data used in this study upon request.

Acknowledgements

The author sincerely thanks MAHE for the financial support through the Dr T. M. A. Pai Doctoral Fellowship. ANP gratefully acknowledges MAHE for the intramural funding (MAHE/CDS/PHD/IMF/2022), which has greatly supported this research.

References

1 S. Yang, Y. Li, L. Deng, S. Tian, Y. Yao, F. Yang, C. Feng, J. Dai, P. Wang and M. Gao, Flexible thermoelectric generator and energy management electronics powered by body heat, *Microsyst. Nanoeng.*, 2023, **9**, 106, DOI: **10.1038/s41378-023-00583-3**.

2 N. Jaziri, A. Boughamoura, J. Müller, B. Mezghani, F. Tounsi and M. Ismail, A comprehensive review of Thermoelectric Generators: Technologies and common applications, *Energy Rep.*, 2020, **6**, 264–287, DOI: **10.1016/j.egyr.2019.12.011**.

3 M. N. Hasan, M. Nafea, N. Nayan and M. S. Mohamed Ali, Thermoelectric Generator: Materials and Applications in Wearable Health Monitoring Sensors and Internet of Things Devices, *Adv. Mater. Technol.*, 2022, **7**, 1–32, DOI: **10.1002/admt.202101203**.

4 L. S. Hewawasam, A. S. Jayasena, M. M. M. Afnan, R. A. C. P. Ranasinghe and M. A. Wijewardane, Waste heat recovery from thermo-electric generators (TEGs), *Energy Rep.*, 2020, **6**, 474–479, DOI: **10.1016/j.egyr.2019.11.105**.

5 X. Cai, X. Fan, Z. Rong, F. Yang, Z. Gan and G. Li, Improved thermoelectric properties of Bi2Te3-xSe x alloys by melt spinning and resistance pressing sintering, *J. Phys. D Appl. Phys.*, 2014, **47**, 115101, DOI: **10.1088/0022-3727/47/11/115101**.

6 A. Bali, H. Wang, G. J. Snyder and R. C. Mallik, Thermoelectric properties of indium doped PbTe1-ySey alloys, *J. Appl. Phys.*, 2014, **116**, 0–7, DOI: **10.1063/1.4890320**.

7 M. Chen, Z. Mao, Y. Ji, P. an Zong and Q. Zhang, Bi2Te3-based flexible thermoelectrics, *Mater. Today Energy*, 2024, **44**, 101643, DOI: **10.1016/j.mtener.2024.101643**.

8 K. Mitchell, J. Park, A. Resnick, H. Horner and E. B. Farfan, Phonon scattering and thermal conductivity of actinide oxides with defects, *Appl. Sci.*, 2020, **10**, 1860, DOI: **10.3390/app10051860**.

9 H. Zhu, R. He, J. Mao, Q. Zhu, C. Li, J. Sun, W. Ren, Y. Wang, Z. Liu, Z. Tang, A. Sotnikov, Z. Wang, D. Broido, D. J. Singh, G. Chen, K. Nielsch and Z. Ren, Discovery of ZrCoBi based half Heuslers with high thermoelectric conversion efficiency, *Nat. Commun.*, 2018, **9**, 1–9, DOI: **10.1038/s41467-018-04958-3**.

10 A. Li, Y. Wang, Y. Li, X. Yang, P. Nan, K. Liu, B. Ge, C. Fu and T. Zhu, High performance magnesium-based plastic semiconductors for flexible thermoelectrics, *Nat. Commun.*, 2024, **15**, 5108, DOI: **10.1038/s41467-024-49440-5**.

11 X. Li, C. Chen, W. Xue, S. Li, F. Cao, Y. Chen, J. He, J. Sui, X. Liu, Y. Wang and Q. Zhang, N-type Bi-doped SnSe Thermoelectric Nanomaterials Synthesized by a Facile Solution Method, *Inorg. Chem.*, 2018, **57**, 13800–13808, DOI: **10.1021/acs.inorgchem.8b02324**.

12 A. T. Duong, V. Q. Nguyen, G. Duvjir, V. T. Duong, S. Kwon, J. Y. Song, J. K. Lee, J. E. Lee, S. Park, T. Min, J. Lee, J. Kim and S. Cho, Achieving ZT=2.2 with Bi-doped n-type SnSe single crystals, *Nat. Commun.*, 2016, **7**, 1–6, DOI: **10.1038/ncomms13713**.

13 R. Mori, Y. Mayuzumi, M. Yamaguchi, A. Kobayashi, Y. Seki and M. Takashiri, Improved thermoelectric properties of solvothermally synthesized Bi2Te3 nanoplate films with homogeneous interconnections using Bi2Te3 electrodeposited layers, *J. Alloys Compd.*, 2020, **818**, 152901, DOI: **10.1016/j.jallcom.2019.152901**.

14 W. Xie, J. He, S. Zhu, T. Holgate, S. Wang, X. Tang, Q. Zhang and T. M. Tritt, Investigation of the sintering pressure and thermal conductivity anisotropy of melt-spun spark-plasma-sintered (Bi,Sb)2Te3 thermoelectric materials, *J. Mater. Res.*, 2011, **26**, 1791–1799, DOI: **10.1557/jmr.2011.170**.

15 J. K. Das and M. A. I. Nahid, Electrical Properties of Thermal Evaporated Bismuth Telluride Thin Films, *International Journal of Thin Film Science and Technology*, 2015, **4**(1), 13–16, DOI: **10.12785/ijtfst/040103**.

16 M. R. Shankar, A. N. Prabhu, A. M. Ashok, N. Davis, B. Srinivasan and V. Mishra, Role of Bi/Te co-dopants on the thermoelectric properties of SnSe polycrystals: an experimental and theoretical investigation, *J. Mater. Sci.*, 2024, **59**, 13055–13077, DOI: **10.1007/s10853-024-09984-9**.

17 R. Nayak, P. Shetty, S. M, A. Rao, S. K V, S. Wagle, S. Nayak, V. Kamath, N. Shetty and M. Saquib, Formulation and

optimization of copper selenide/PANI hybrid screen printing ink for enhancing the power factor of flexible thermoelectric generator: A synergetic approach, *Ceram. Int.*, 2024, **50**(14), 25779–25791, DOI: 10.1016/j.ceramint.2024.04.315.

18 R. Nayak, P. Shetty, S. M, A. Rao, K. M. Rao, G. K and S. Mangavati, Enhancement of power factor of screen printed polyaniline/graphite based flexible thermoelectric generator by structural modifications, *J. Alloys Compd.*, 2022, **922**, 166298, DOI: 10.1016/j.jallcom.2022.166298.

19 Z. Cao, E. Koukharenko, M. J. Tudor, R. N. Torah and S. P. Beeby, Screen printed flexible Bi2Te3-Sb2Te 3 based thermoelectric generator, *J. Phys.:Conf. Ser.*, 2013, **476**, 2–7, DOI: 10.1088/1742-6596/476/1/012031.

20 M. R. Shankar, A. N. Prabhu, R. Nayak and M. Saquib, Optimization of thermoelectric parameters in Ag/MnO_2 nanocomposite-based flexible thermoelectric generators, *Ceram. Int.*, 2025, **51**(9), 11821–11833, DOI: 10.1016/j.ceramint.2025.01.035.

21 R. Nayak, P. Shetty, M. Selvakumar, B. Shivamurthy, A. Rao, K. V. Sriram, M. S. Murari, A. Kompa and U. Deepika Shanubhogue, Influence of microstructure and thermoelectric properties on the power density of multi-walled carbon nanotube/metal oxide hybrid flexible thermoelectric generators, *Ceram. Int.*, 2023, **49**, 39307–39328, DOI: 10.1016/j.ceramint.2023.09.275.

22 J. Pang, X. Zhang, L. Shen, J. Xu, Y. Nie and G. Xiang, Synthesis and thermoelectric properties of Bi-doped SnSe thin films, *Chin. Phys. B*, 2022, **30**(11), 116302, DOI: 10.1088/1674-1056/ac11da.

23 V. Q. Nguyen, T. H. Nguyen, V. T. Duong, J. E. Lee, S. D. Park, J. Y. Song, H. M. Park, A. T. Duong and S. Cho, Thermoelectric Properties of Hot-Pressed Bi-Doped n-Type Polycrystalline SnSe, *Nanoscale Res. Lett.*, 2018, **13**, 4–10, DOI: 10.1186/s11671-018-2500-y.

24 S. Chen, K. Cai and W. Zhao, The effect of Te doping on the electronic structure and thermoelectric properties of SnSe, *Phys. B*, 2012, **407**, 4154–4159, DOI: 10.1016/j.physb.2012.06.041.

25 S. A. Disha, M. Sahadat Hossain, M. L. Habib and S. Ahmed, Calculation of crystallite sizes of pure and metals doped hydroxyapatite engaging Scherrer method, Halder-Wagner method, Williamson-Hall model, and size-strain plot, *Results Mater.*, 2024, **21**, 100496, DOI: 10.1016/j.rinma.2023.100496.

26 J. Gao, H. Zhu, T. Mao, L. Zhang, J. Di and G. Xu, The effect of Sm doping on the transport and thermoelectric properties of SnSe, *Mater. Res. Bull.*, 2017, **93**, 366–372, DOI: 10.1016/j.materresbull.2017.04.053.

27 J. R. Watling and D. J. Paul, A study of the impact of dislocations on the thermoelectric properties of quantum wells in the Si/SiGe materials system, *J. Appl. Phys.*, 2011, **110**(11), 114508, DOI: 10.1063/1.3665127.

28 Q. K. Zhang, S. T. Ning, N. Qi, Z. Q. Chen, X. F. Tang and Z. Y. Chen, Enhanced thermoelectric performance of a simple method prepared polycrystalline SnSe optimized by spark plasma sintering, *J. Appl. Phys.*, 2019, **125**(22), 225109, DOI: 10.1063/1.5095197.

29 K. Kothari and M. Maldovan, Phonon Surface Scattering and Thermal Energy Distribution in Superlattices, *Sci. Rep.*, 2017, **7**, 1–15, DOI: 10.1038/s41598-017-05631-3.

30 N. K. Singh, S. Bathula, B. Gahtori, K. Tyagi, D. Haranath and A. Dhar, The effect of doping on thermoelectric performance of p-type SnSe: Promising thermoelectric material, *J. Alloys Compd.*, 2016, **668**, 152–158, DOI: 10.1016/j.jallcom.2016.01.190.

31 C. Purushottam Bhat, Anusha, A. Ani, U. D. Shanubhogue, P. Poornesh, A. Rao and S. Chattopadhyay, Investigations on Bi Doped Cu2Se Prepared by Solid State Reaction Technique for Thermoelectric Applications, *Energies*, 2023, **16**(7), 3010, DOI: 10.3390/en16073010.

32 D. Sidharth, A. S. Alagar Nedunchezhian, R. Rajkumar, N. Yalini Devi, P. Rajasekaran, M. Arivanandhan, K. Fujiwara, G. Anbalagan and R. Jayavel, Enhancing effects of Te substitution on the thermoelectric power factor of nanostructured SnSe1-: XTex, *Phys. Chem. Chem. Phys.*, 2019, **21**, 15725–15733, DOI: 10.1039/c9cp02018g.

33 J. Zhou, H. Zhu, Q. Song, Z. Ding, J. Mao, Z. Ren and G. Chen, Mobility enhancement in heavily doped semiconductors *via* electron cloaking, *Nat. Commun.*, 2022, **13**, 1–10, DOI: 10.1038/s41467-022-29958-2.

34 Y. S. Wudil, M. A. Gondal, M. A. Almessiere and A. Q. Alsayoud, The multi-dimensional approach to synergistically improve the performance of inorganic thermoelectric materials: A critical review, *Arabian J. Chem.*, 2021, **14**, 103103, DOI: 10.1016/j.arabjc.2021.103103.

35 X. Gu, S. Li and H. Bao, Thermal conductivity of silicon at elevated temperature: Role of four-phonon scattering and electronic heat conduction, *Int. J. Heat Mass Transfer*, 2020, **160**, 120165, DOI: 10.1016/j.ijheatmasstransfer.2020.120165.

36 B. Cai, H. Hu, H. L. Zhuang and J. F. Li, Promising materials for thermoelectric applications, *J. Alloys Compd.*, 2019, **806**, 471–486, DOI: 10.1016/j.jallcom.2019.07.147.

37 V. Karthikeyan, T. Li, B. Medasani, C. Luo, D. Shi, J. C. K. Wong, K. H. Lam, F. C. C. Ling and V. A. L. Roy, Defect and Dopant Mediated Thermoelectric Power Factor Tuning in β-Zn4Sb3, *Adv. Electron. Mater.*, 2020, **6**, 1–9, DOI: 10.1002/aelm.201901284.

38 F. Li, W. Wang, X. Qiu, Z. Zheng, P. Fan, J. Luo and B. Li, Optimization of thermoelectric properties of n-type Ti, Pb co-doped SnSe, *Inorg. Chem. Front.*, 2017, **4**(10), 1721–1729, DOI: 10.1039/c7qi00436b.

39 Q. Yan and M. G. Kanatzidis, High-performance thermoelectrics and challenges for practical devices, *Nat. Mater.*, 2022, **21**, 503–513, DOI: 10.1038/s41563-021-01109-w.

40 Y. Du, K. Cai, S. Chen, H. Wang, S. Z. Shen, R. Donelson and T. Lin, Thermoelectric fabrics: Toward power generating clothing, *Sci. Rep.*, 2015, **5**, 1–6, DOI: 10.1038/srep06411.

41 O. Bubnova, Z. U. Khan, A. Malti, S. Braun, M. Fahlman, M. Berggren and X. Crispin, Optimization of the thermoelectric figure of merit in the conducting polymer poly(3,4-ethylenedioxythiophene), *Nat. Mater.*, 2011, **10**, 429–433, DOI: 10.1038/nmat3012.

42 D. Beretta, M. Massetti, G. Lanzani and M. Caironi, Thermoelectric characterization of flexible micro-thermoelectric generators, *Rev. Sci. Instrum.*, 2017, **88**, 4973417, DOI: **10.1063/1.4973417**.

43 Z. Lu, H. Zhang, C. Mao and C. M. Li, Silk fabric-based wearable thermoelectric generator for energy harvesting from the human body, *Appl. Energy*, 2016, **164**, 57–63, DOI: **10.1016/j.apenergy.2015.11.038**.

44 H. Zhou, Z. Zhang, C. Sun, H. Deng and Q. Fu, Biomimetic Approach to Facilitate the High Filler Content in Free-Standing and Flexible Thermoelectric Polymer Composite Films Based on PVDF and Ag2Se Nanowires, *ACS Appl. Mater. Interfaces*, 2020, **12**, 51506–51516, DOI: **10.1021/acsami.0c15414**.

45 R. Mulla, D. R. Jones and C. W. Dunnill, Thermoelectric Paper: Graphite Pencil Traces on Paper to Fabricate a Thermoelectric Generator, *Adv. Mater. Technol.*, 2020, **5**, 2–9, DOI: **10.1002/admt.202000227**.

46 A. Yadav, K. P. Pipe and M. Shtein, Fiber-based flexible thermoelectric power generator, *J. Power Sources*, 2008, **175**, 909–913, DOI: **10.1016/j.jpowsour.2007.09.096**.

47 Y. H. Kang, S. J. Ko, M. H. Lee, Y. K. Lee, B. J. Kim and S. Y. Cho, Highly efficient and air stable thermoelectric devices of poly(3-hexylthiophene) by dual doping of Au metal precursors, *Nano Energy*, 2021, **82**, 105681, DOI: **10.1016/j.nanoen.2020.105681**.

48 X. L. Huang, D. W. Ao, T. B. Chen, Y. X. Chen, F. Li, S. Chen, G. X. Liang, X. H. Zhang, Z. H. Zheng and P. Fan, High-performance copper selenide thermoelectric thin films for flexible thermoelectric application, *Mater. Today Energy*, 2021, **21**, 100743, DOI: **10.1016/j.mtener.2021.100743**.

49 D. Liu, Z. Yan, Y. Zhao, Z. Zhang, Y. Zheng, B. Zhang, P. Shi and C. Xue, Enhanced performance of SnSe/PEDOT: PSS composite films by MWCNTs for flexible thermoelectric power generator, *J. Alloys Compd.*, 2022, **898**, 162844, DOI: **10.1016/j.jallcom.2021.162844**.